

# Single domain antibody-scFv conjugate targeting amyloid $\beta$ and TfR penetrates the blood–brain barrier and interacts with amyloid $\beta$

Rebecca Faresjö, Elisabet O. Sjöström, Tiffany Dallas, Magnus M. Berglund, Jonas Eriksson, Dag Sehlin & Stina Syvänen

To cite this article: Rebecca Faresjö, Elisabet O. Sjöström, Tiffany Dallas, Magnus M. Berglund, Jonas Eriksson, Dag Sehlin & Stina Syvänen (2024) Single domain antibody-scFv conjugate targeting amyloid  $\beta$  and TfR penetrates the blood–brain barrier and interacts with amyloid  $\beta$ , mAbs, 16:1, 2410968, DOI: [10.1080/19420862.2024.2410968](https://doi.org/10.1080/19420862.2024.2410968)

To link to this article: <https://doi.org/10.1080/19420862.2024.2410968>



© 2024 The Author(s). Published with license by Taylor & Francis Group, LLC.



View supplementary material [↗](#)



Published online: 02 Oct 2024.



Submit your article to this journal [↗](#)



Article views: 1261



View related articles [↗](#)





View Crossmark data [↗](#)

REPORT



# Single domain antibody-scFv conjugate targeting amyloid $\beta$ and TfR penetrates the blood–brain barrier and interacts with amyloid $\beta$

Rebecca Faresjö<sup>a</sup>, Elisabet O. Sjöström<sup>a,b</sup>, Tiffany Dallas<sup>a,b</sup>, Magnus M. Berglund<sup>b</sup>, Jonas Eriksson<sup>c,d</sup>, Dag Sehlin<sup>d</sup>, and Stina Syvänen<sup>d</sup>

<sup>a</sup>Department of Public Health and Caring Sciences, Uppsala University, Uppsala, Sweden; <sup>b</sup>Key2Brain AB, Solna, Sweden; <sup>c</sup>PET Centre, Uppsala University Hospital, Uppsala, Sweden; <sup>d</sup>Department of Medicinal Chemistry, Uppsala University, Sweden

## ABSTRACT

Neurodegenerative diseases such as Alzheimer's disease (AD) pose substantial challenges to patients and health-care systems, particularly in countries with aging populations. Immunotherapies, including the marketed antibodies lecanemab (Leqembi<sup>®</sup>) and donanemab (Kisunla<sup>TM</sup>), offer promise but face hurdles due to limited delivery across the blood–brain barrier (BBB). This limitation necessitates high doses, resulting in increased costs and a higher risk of side effects. This study explores transferrin receptor (TfR)-binding camelid single-domain antibodies (VHHs) for facilitated brain delivery. We developed and evaluated fusion proteins (FPs) combining VHHs with human IgG Fc domains or single-chain variable fragments (scFvs) of the anti-amyloid-beta (A $\beta$ ) antibody 3D6. *In vitro* assessments showed varying affinities of the FPs for TfR. *In vivo* evaluations indicated that specific VHH-Fc and VHH-scFv fusions reached significant brain concentrations, emphasizing the importance of optimal TfR binding affinities. The VHH-scFv fusions were further investigated in mouse models with A $\beta$  pathology, showing higher retention compared to wild-type mice without A $\beta$  pathology. Our findings suggest that these novel VHH-based FPs hold potential for therapeutic and diagnostic applications in AD, providing a strategy to overcome BBB limitations and enhance brain targeting of antibody-based treatments. Furthermore, our results suggest that a given bispecific TfR-binding fusion format has a window of “optimal” affinity where parenchymal delivery is adequate, while blood pharmacokinetics aligns with the desired application of the fusion protein.

## ARTICLE HISTORY

Received 8 July 2024  
Revised 5 September 2024  
Accepted 25 September 2024

## KEYWORDS

Blood-brain barrier; brain delivery; camelid antibody; fusion protein; transferrin receptor; VHH

## Introduction



Neurodegenerative diseases, such as Alzheimer's disease (AD), are associated with an increasing number of patients, posing burdens to the families and relatives of those affected and significant societal costs. Recognized as a public health crisis, the prevalence of AD and other neurodegenerative diseases is expected to increase in the coming decades due to the aging populations of many countries. Consequently, there is an urgent need for early detection and effective therapeutic interventions to address this growing challenge.


Immunotherapy, specifically treatments based on antibodies, is currently one of the most promising treatment options for AD. In 2023, the antibody lecanemab (Leqembi<sup>®</sup>), which targets amyloid-beta (A $\beta$ ) aggregates, was approved by the US Food and Drug Administration (FDA).<sup>1</sup> Additionally, several other similar antibodies are being studied in late-phase clinical trials, including antibody donanemab (Kisunla<sup>TM</sup>), which was FDA-approved in 2024.<sup>2,3</sup> However, antibodies show restricted delivery across the blood–brain barrier (BBB). Typically, less than 0.1% of systemically administered monoclonal antibodies (mAbs) (~150 kDa) reach the brain, with the maximum brain concentration (C<sub>max</sub>) only reached days after administration.<sup>4–8</sup> The slow and low brain delivery necessitates

large doses, which is both costly and likely to produce side effects due to high antibody concentrations in the periphery.

One strategy to enhance brain delivery of antibodies involves receptor-mediated transcytosis (RMT), with the transferrin receptor 1 (TfR1, hereafter TfR) being the most widely used and clinically validated receptor for this purpose. We have established that fusing antibodies with a murine TfR-specific (mTfR) single-chain variable fragment, scFv8D3, significantly increases brain concentrations of lecanemab and other therapeutic antibodies in mice.<sup>5,9</sup> These bispecific antibodies also show rapid brain delivery. Furthermore, we have demonstrated that, after radiolabeling, the bispecific mTfR-A $\beta$  antibodies can be used as positron emission tomography (PET) radioligands to detect A $\beta$  pathology in mouse models of AD.<sup>10–15</sup> For PET, smaller-sized bispecific formats are desirable. These formats are associated with fast systemic clearance, ideally lack the crystallizable fragment (Fc) domain, which avoids immune reactions and recycling of cell-internalized antibodies. Rapid clearance may be facilitated if the bispecific antibody is small (~60 kDa or less) and thus can be excreted via the kidneys because it is below the size limit for glomerular filtration.<sup>9,16,17</sup>

A promising approach to create small TfR-binders for fusion to, e.g., A $\beta$  binding antibodies or antibody fragments,

**CONTACT** Stina Syvänen  [stina.syvanen@uu.se](mailto:stina.syvanen@uu.se)  Department of Public Health and Caring Sciences, Uppsala University, Rudbeck Laboratory, Dag Hammarskjölds väg 20, Uppsala SE-75185, Sweden

 Supplemental data for this article can be accessed online at <https://doi.org/10.1080/19420862.2024.2410968>

© 2024 The Author(s). Published with license by Taylor & Francis Group, LLC.

This is an Open Access article distributed under the terms of the Creative Commons Attribution License (<http://creativecommons.org/licenses/by/4.0/>), which permits unrestricted use, distribution, and reproduction in any medium, provided the original work is properly cited. The terms on which this article has been published allow the posting of the Accepted Manuscript in a repository by the author(s) or with their consent.

involves use of the variable domain of heavy-chain antibodies derived from camelids. These single heavy chain domain fragments (VHHs), with a molecular weight of 12–15 kDa, offer high target specificity and fast blood clearance. Compared to other small antibody fragments, such as Fab (~50 kDa) or scFvs (~25 kDa), VHHs are smaller, which can allow binding to epitopes that are hidden from larger antibodies,<sup>18</sup> more stable, and easily expressed recombinantly. Several studies have shown the potential of strategies to increase the BBB penetration of VHHs, or cargos thereof,<sup>19–22</sup> but, to transition preclinical proteins to clinical use, they must be translatable across species. Most antibodies designed for brain delivery via TfR transport target the apical domain of TfR to avoid interfering with endogenous transfer in binding.<sup>6,23,24</sup> Since the TfR apical domain is only around 70% identical between mice and humans, most TfR binders are species-specific.<sup>21,25</sup> Therefore, developing novel TfR binders that specifically target the human TfR (hTfR), including further exploration of optimal binding characteristics, are valuable for clinical applications. Strategies include using knock-in mouse models expressing hTfR or developing cross-species reactive TfR binders, such as single-domain shark antibody fragments (VNARs) or camelid VHHs.<sup>6,26–29</sup> However, generating cross-species reactive TfR binders with similar affinities for both mTfR and hTfR has proven challenging. Optimal binding affinity to TfR is crucial for transport efficiency: low or intermediate affinity and monovalent binding are advantageous for therapeutic dosing, while slightly higher affinity may benefit low-dose applications.<sup>23,30,31</sup>

In this study, we present novel VHH TfR-binders, including human-mouse cross-species reactive variants and the successful production of fusion proteins (FPs), wherein the TfR-binding VHH is fused to either an Fc-domain or the scFv of the A $\beta$  antibody 3D6 (scFv3D6). We further describe their ability to target pathology in a mouse model of A $\beta$  pathology, with the aim of advancing these novel TfR-binders for future therapeutic and diagnostic applications.

## Results

### Expression and in vitro evaluation of fusion proteins

Three novel TfR-binding VHHs, along with one previously published TfR-binding VHH, were produced as VHH-Fc fusion proteins (FP<sub>Fc</sub>). The VHHs were genetically fused to the N-terminus of both chains of a human IgG Fc domain, creating a stable IgG-like fusion protein of 75 kDa for initial evaluation. The following FPs were designed and expressed (see also Table 1): one cross-species reactive for mTfR/hTfR (FP<sub>Fc</sub>1), one binding only to the mTfR (FP<sub>Fc</sub>2), one binding only to the hTfR (FP<sub>Fc</sub>3), and a reference, cross-species reactive benchmark construct (FP<sub>Fc</sub>4), with the VHH used herein being based on a characterized sequence in patent WO 2020/144233.<sup>26</sup>

After initial evaluation with the four FP<sub>Fc</sub>, the VHHs were fused to the scFv domain of 3D6 to produce small bispecific fusion proteins (FP<sub>scFv</sub>) that bind monovalently to TfR and to A $\beta$  (Figure 1).<sup>5,32</sup> The variable heavy (VH) and variable light (VL) chains of scFv3D6 were connected with a 3 × (Gly<sub>4</sub>Ser)-linker. An identical linker was used to connect VHHs to

**Table 1.** Description of fusion proteins and their short names.

Description	Short name
VHH1-Fc	FP <sub>Fc</sub> 1
VHH2-Fc	FP <sub>Fc</sub> 2
VHH3-Fc	FP <sub>Fc</sub> 3
VHH4-Fc	FP <sub>Fc</sub> 4
scFv3D6-VHH1	FP <sub>scFv</sub> 1A
VHH1-scFv3D6	FP <sub>scFv</sub> 1B
scFv3D6-VHH2	FP <sub>scFv</sub> 2A
VHH2-scFv3D6	FP <sub>scFv</sub> 2B
scFv3D6-VHH3	FP <sub>scFv</sub> 3A
VHH3-scFv3D6	FP <sub>scFv</sub> 3B
scFv3D6-VHH4	FP <sub>scFv</sub> 4A
VHH4-scFv3D6	FP <sub>scFv</sub> 4B

Note: FP = fusion protein.

scFv3D6. The VHHs were fused either to the C- or N-terminus of scFv3D6, denoted as “A” or “B” orientation, respectively (Table 1, Figure 1).

The FPs were studied by enzyme-linked immunosorbent assay (ELISA) to determine their binding to mTfR and hTfR. The cross-species reactive FP<sub>Fc</sub>1 and FP<sub>Fc</sub>4, exhibited binding to both mTfR and hTfR, with higher binding to hTfR (Figure 2a i, iv). All VHH2-based constructs showed selective mTfR binding, while VHH3-based proteins bound exclusively to hTfR. The fusion of a single VHH (a monovalent TfR construct) to scFv3D6 decreased the total binding for the cross-species reactive FP<sub>scFv</sub>1 and FP<sub>scFv</sub>4, compared with that of the bivalently binding FP<sub>Fc</sub>1 and FP<sub>Fc</sub>4, with more pronounced loss of binding to mTfR compared with hTfR (Figure 2a–c i for FP1-based proteins and 2 a–c iv for FP4-based proteins). The affinity of VHH2 and VHH3 was only modestly affected by fusion to scFv3D6, as evaluated by ELISA (Figure 2b–c, ii–iii). The FP<sub>scFv</sub>1B and FP<sub>scFv</sub>4B (Figure 2c i and iv) constructs had slightly better *in vitro* binding profiles compared to FP<sub>scFv</sub>1A and FP<sub>scFv</sub>4A, respectively (Figure 2b i and iv). The binding of the scFv8D3 moiety to A $\beta$  was not influenced by the orientation of the fusion. (Supplementary Fig S1).

The kinetic binding data for all FPs, obtained by surface plasmon resonance (SPR) analyses, are presented in Table 2. Representative sensorgrams for the human–mouse reactive FPs are shown in Figures 2d, 2e. The data agreed with the ELISA results, indicating that FP<sub>Fc</sub>1, as a bivalent Fc-fusion, binds to hTfR with very high avidity (0.067 nM) and to the mTfR with a  $K_D$  of 11 nM. When fused with scFv3D6,  $K_D$  values for interaction with the hTfR were 1.8 and 0.84 nM for FP<sub>scFv</sub>1A and FP<sub>scFv</sub>1B, respectively, and for the mTfR, 23 and 19 nM, respectively. The bivalent FP<sub>Fc</sub>4 bound to hTfR with extreme avidity (0.00053 nM, in fact below the measurable range for dissociation, (Figure 2e, 2i) and also the mTfR with very high avidity, with an equilibrium dissociation constant ( $K_D$ ) of 0.27 nM. When fused with scFv3D6, the  $K_D$  values were 0.70 and 0.19 nM for FP<sub>scFv</sub>4A and FP<sub>scFv</sub>4B, respectively (Table 2). FP<sub>Fc</sub>2, FP<sub>scFv</sub>2A and FP<sub>scFv</sub>2B did not bind hTfR and FP<sub>Fc</sub>3 did not bind mTfR (data not shown), thus confirming the TfR specificities of the FPs demonstrated by ELISA.

### Ex vivo evaluation of Fc-fusion proteins

Radiolabeled FP<sub>Fc</sub> constructs were evaluated *ex vivo* 2.5 h after injection in wild-type (WT) mice. The hTfR binder [<sup>125</sup>

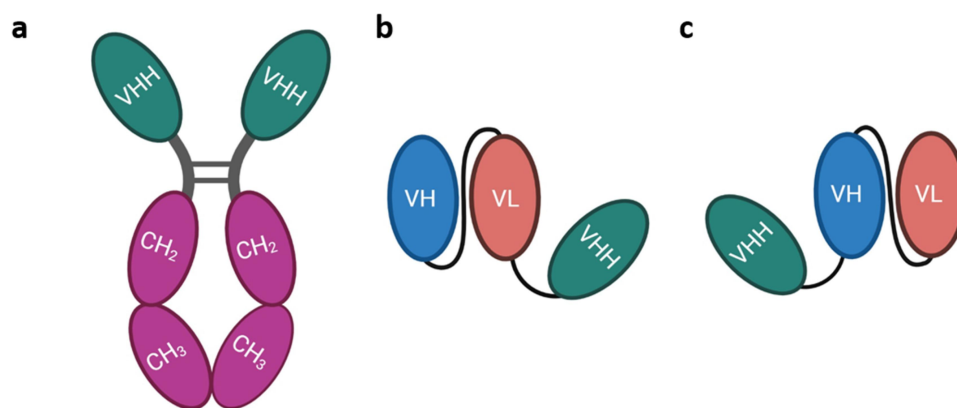


**Figure 1.** Schematic illustration of the different fusion protein formats in the paper. a) two VHH fused with human fc domain; FP<sub>Fc</sub>. b) single VHH fused to the C-terminus of scFv3d6; FP<sub>scFvA</sub>. c) single VHH fused to the N-terminus of scFv3d6; FP<sub>scFvB</sub>.

I]FP<sub>Fc3</sub>, lacking affinity for the mTfR, showed the highest blood concentration at this time point. The lower-affinity cross-species reactive [<sup>125</sup>I]FP<sub>Fc1</sub>, displayed higher blood concentrations compared with the high-affinity mTfR binder [<sup>125</sup>I]FP<sub>Fc2</sub> and the cross-species reactive [<sup>125</sup>I]FP<sub>Fc4</sub> (Figure 3a). Given that blood cells express TfR and could potentially lower the concentration of FP available for delivery to the brain and other organs, it was also important to measure the fraction of FPs remaining in the plasma after blood cells were removed by centrifugation of the samples. The fraction present in plasma was above 60% for all FP<sub>Fc</sub> constructs, but notably it was significantly higher for the hTfR binding [<sup>125</sup>I]FP<sub>Fc3</sub> compared with the high-affinity mTfR binding [<sup>125</sup>I]FP<sub>Fc2</sub> (Figure 3b). The blood concentration profiles showed that mTfR binders appeared to exhibit faster elimination from blood in WT mice compared with the hTfR binder [<sup>125</sup>I]FP<sub>Fc3</sub> (Figure 3c).

The [<sup>125</sup>I]FP<sub>Fc1</sub> displayed a total brain concentration of  $1.2 \pm 0.3\%ID/g_{\text{brain}}$ , which was lower than that observed for [<sup>125</sup>I]FP<sub>Fc4</sub> and [<sup>125</sup>I]FP<sub>Fc2</sub>, which both exhibited similar brain concentrations of  $2.8 \pm 0.2$  and  $2.9 \pm 0.2\%ID/g_{\text{brain}}$ , respectively (Figure 3d). The hTfR binder [<sup>125</sup>I]FP<sub>Fc3</sub>, had very low brain concentrations in WT mice,  $0.17 \pm 0.04\%ID/g_{\text{brain}}$ . Brain-to-blood ratios were higher for [<sup>125</sup>I]FP<sub>Fc4</sub> and [<sup>125</sup>I]FP<sub>Fc2</sub>, compared with [<sup>125</sup>I]FP<sub>Fc1</sub> (Figure 3e). Again, hTfR binder [<sup>125</sup>I]FP<sub>Fc3</sub> showed a very low brain-to-blood ratio, as expected for a non-brain targeting protein. The distribution to the liver and spleen was especially high for [<sup>125</sup>I]FP<sub>Fc2</sub>, while [<sup>125</sup>I]FP<sub>Fc1</sub> had lower distribution to these organs compared with [<sup>125</sup>I]FP<sub>Fc2</sub> and [<sup>125</sup>I]FP<sub>Fc4</sub>, and the hTfR binder [<sup>125</sup>I]FP<sub>Fc3</sub> (Figure 3f). The hTfR binder [<sup>125</sup>I]FP<sub>Fc3</sub> showed limited distribution to the bone, likely due to its lack of binding to mTfR expressed by the bone marrow.

In contrast to what was observed in WT mice that harbor the mTfR/mTfR genotype, the hTfR binder [<sup>125</sup>I]FP<sub>Fc3</sub> displayed the fastest elimination from blood and the highest brain delivery in mice homozygous for the hTfR (Figure 4). Thus, in homozygous hTfR mice, [<sup>125</sup>I]FP<sub>Fc3</sub> displayed brain delivery similar to that seen with mTfR binder [<sup>125</sup>I]FP<sub>Fc2</sub> in WT mice.

### Characterization of brain distribution of Fc-fusion proteins

In WT mice, the mTfR-binding FP<sub>Fc</sub> constructs [<sup>125</sup>I]FP<sub>Fc1</sub>, [<sup>125</sup>I]FP<sub>Fc2</sub>, and [<sup>125</sup>I]FP<sub>Fc4</sub> were present in the brain capillaries (as demonstrated by CD31-positivity), in contrast to the hTfR binder [<sup>125</sup>I]FP<sub>Fc3</sub> (Figure 5 a–d). The mTfR-specific [<sup>125</sup>I]FP<sub>Fc2</sub> had the highest association with mouse brain capillaries (Figure 5b). Parenchymal (non-vascular) signal was also more evident for the mTfR binders compared with the hTfR-binder [<sup>125</sup>I]FP<sub>Fc3</sub>.

### Ex vivo evaluation of scFv3D6-fusion proteins at 2 h post-injection

Similar to the studies of the FP<sub>Fc</sub> constructs, the FP<sub>scFv</sub> constructs were evaluated at 2 h post-injection to investigate brain delivery. The FP<sub>scFv</sub> constructs fused to the C-terminus of scFv3D6 (denoted with A) were compared with those fused to the N-terminus of scFv3D6 (denoted with B).

Blood concentrations at 2 h after injections were lower for [<sup>125</sup>I]FP<sub>scFv1A</sub> and [<sup>125</sup>I]FP<sub>scFv4A</sub> compared with [<sup>125</sup>I]FP<sub>scFv1B</sub> and [<sup>125</sup>I]FP<sub>scFv4B</sub> (Figure 6a). Overall, the distribution to plasma was slightly lower compared to the respective Fc fusion and [<sup>125</sup>I]FP<sub>scFv4B</sub> and [<sup>125</sup>I]FP<sub>scFv2B</sub> displayed particularly low relative distribution to plasma (Figure 6b).

Overall, total brain concentrations at 2 h post-injection were lower for the TfR monovalent binding FP<sub>scFv</sub> constructs compared to the previously studied bivalent Fc-constructs. Further, [<sup>125</sup>I]FP<sub>scFv1B</sub> displayed significantly (3-fold) higher brain concentrations than [<sup>125</sup>I]FP<sub>scFv1A</sub>, indicating that the fusion to the C-terminal end of scFv3D6 attenuated TfR binding (Figure 6c, Supplementary Table S1). The same was observed for FP<sub>scFv4</sub>, where [<sup>125</sup>I]FP<sub>scFv4B</sub> had 2-fold higher brain concentrations than [<sup>125</sup>I]FP<sub>scFv4A</sub>. The mTfR binder FP<sub>scFv2</sub> was least affected by the orientation of the fusion, displaying similar brain concentrations for [<sup>125</sup>I]FP<sub>scFv2A</sub> and [<sup>125</sup>I]FP<sub>scFv2B</sub>. Except for [<sup>125</sup>I]FP<sub>scFv1A</sub>, all FP<sub>scFv</sub> constructs directed toward mTfR, showed substantially higher brain concentrations compared with the hTfR binding [<sup>125</sup>I]FP<sub>scFv3B</sub>, indicating maintained mTfR *in vivo* binding after scFv3D6 fusion and radiolabeling.

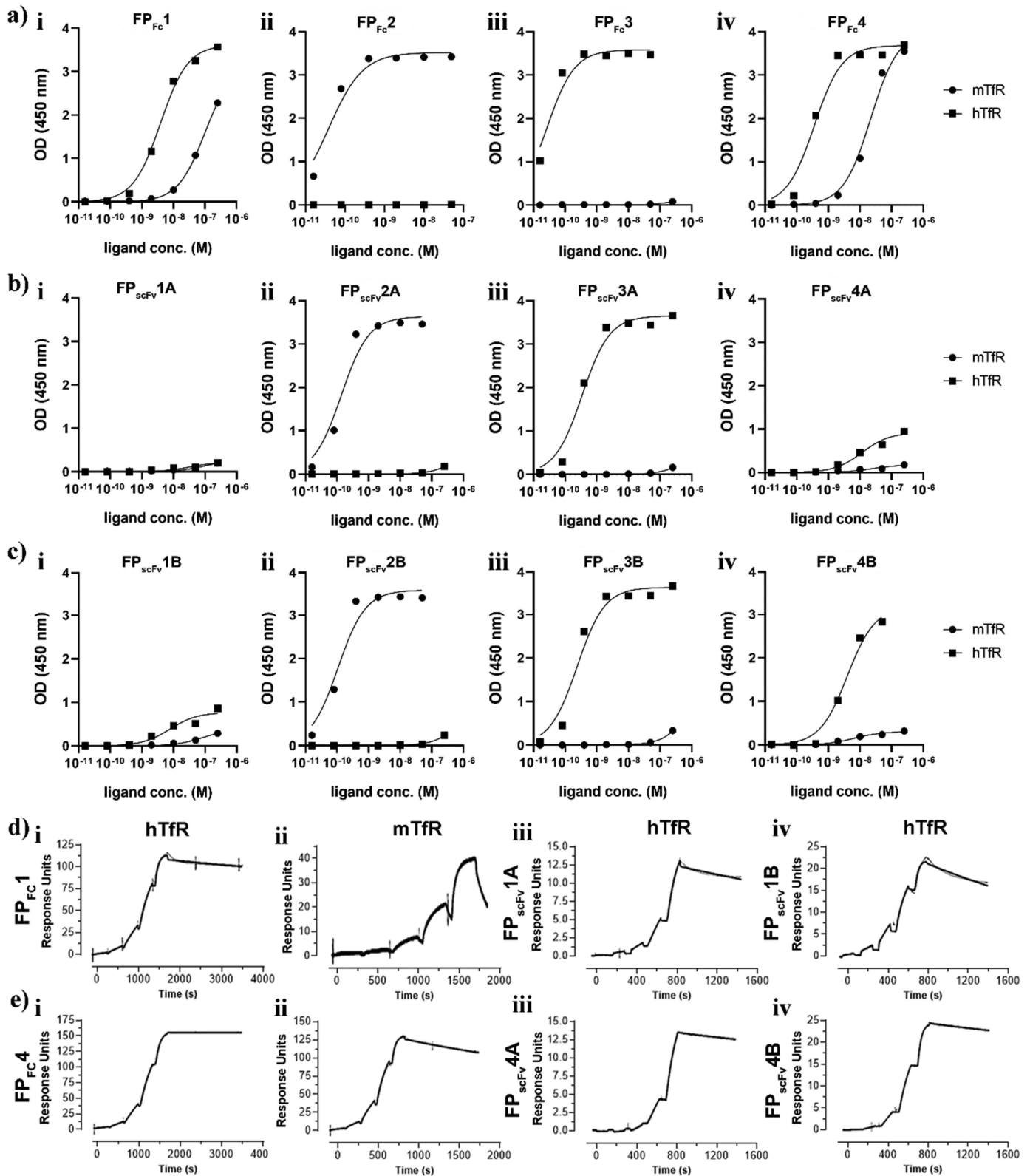


**Figure 2.** a) ELISA binding profiles for constructs in the format of fc fusions i) FP<sub>Fc</sub>1, ii) FP<sub>Fc</sub>2, iii) FP<sub>Fc</sub>3 and iv) FP<sub>Fc</sub>4 to mTfR and hTfR b) ELISA binding profiles for fusions of the scFv-vhh orientation i) FP<sub>scFv</sub>1A, ii) FP<sub>scFv</sub>2A, iii) FP<sub>scFv</sub>3A and iv) FP<sub>scFv</sub>4A c) binding profiles for the fusions of the vhh-scFv orientation i) FP<sub>scFv</sub>1B, ii) FP<sub>scFv</sub>2B, iii) FP<sub>scFv</sub>3B and iv) FP<sub>scFv</sub>4B d) sensorgrams for VHH1 in the format as fc fusion (FP<sub>Fc</sub>1) binding to i) hTfR, ii) mTfR and in the format as fusions to anti- $\beta$  scFv3d6, iii) scFv-vhh orientation: FP<sub>scFv</sub>1A and iv) vhh-scFv orientation: FP<sub>scFv</sub>4A e) sensorgrams for VHH4 in the format as fc fusion (FP<sub>Fc</sub>4) binding to i) hTfR, ii) mTfR and in the format as fusion to anti- $\beta$  scFv3d6, iii) scFv-vhh orientation: FP<sub>scFv</sub>4A and VHH-scFv orientation: FP<sub>scFv</sub>4B. The receptors were immobilized by amine coupling on a CM5 chip.

**Table 2.** SPR kinetic binding parameters. Association rate constant,  $k_a$ ; dissociation rate constant,  $k_d$ ; equilibrium dissociation constant,  $K_D$ .

Construct	TfR species	$k_a$ ( $M^{-1}s^{-1}$ )	$k_d$ ( $s^{-1}$ )	$K_D$ (nM)
FP <sub>Fc</sub> 1	human	$6.51 \times 10^5$	$4.34 \times 10^{-5}$	0.067
FP <sub>Fc</sub> 1	mouse	$3.54 \times 10^5$	$3.83 \times 10^{-3}$	11
FP <sub>scFv</sub> 1A	human	$1.44 \times 10^5$	$2.59 \times 10^{-4}$	1.8
FP <sub>scFv</sub> 1B	human	$5.35 \times 10^5$	$4.50 \times 10^{-4}$	0.84
FP <sub>scFv</sub> 1A	mouse	$1.42 \times 10^5$	$3.28 \times 10^{-3}$	23
FP <sub>scFv</sub> 1B	mouse	$5.17 \times 10^5$	$9.70 \times 10^{-3}$	19
FP <sub>Fc</sub> 2	mouse	$1.22 \times 10^5$	$6.74 \times 10^{-5}$	0.55
FP <sub>scFv</sub> 2A	mouse	$5.43 \times 10^5$	$1.30 \times 10^{-3}$	4.1
FP <sub>scFv</sub> 2B	mouse	$4.89 \times 10^5$	$2.01 \times 10^{-3}$	5.4
FP <sub>Fc</sub> 3	human	$8.01 \times 10^5$	$6.49 \times 10^{-5}$	0.081
FP <sub>scFv</sub> 3A	human	$9.25 \times 10^5$	$4.77 \times 10^{-3}$	5.2
FP <sub>scFv</sub> 3B	human	$7.77 \times 10^5$	$4.40 \times 10^{-3}$	6.5
FP <sub>Fc</sub> 4	human	$5.38 \times 10^5$	$2.86 \times 10^{-7}$	0.00053
FP <sub>Fc</sub> 4	mouse	$3.38 \times 10^5$	$9.09 \times 10^{-5}$	0.27
FP <sub>scFv</sub> 4A	human	$1.75 \times 10^5$	$1.22 \times 10^{-4}$	0.70
FP <sub>scFv</sub> 4B	human	$6.17 \times 10^5$	$1.17 \times 10^{-4}$	0.19

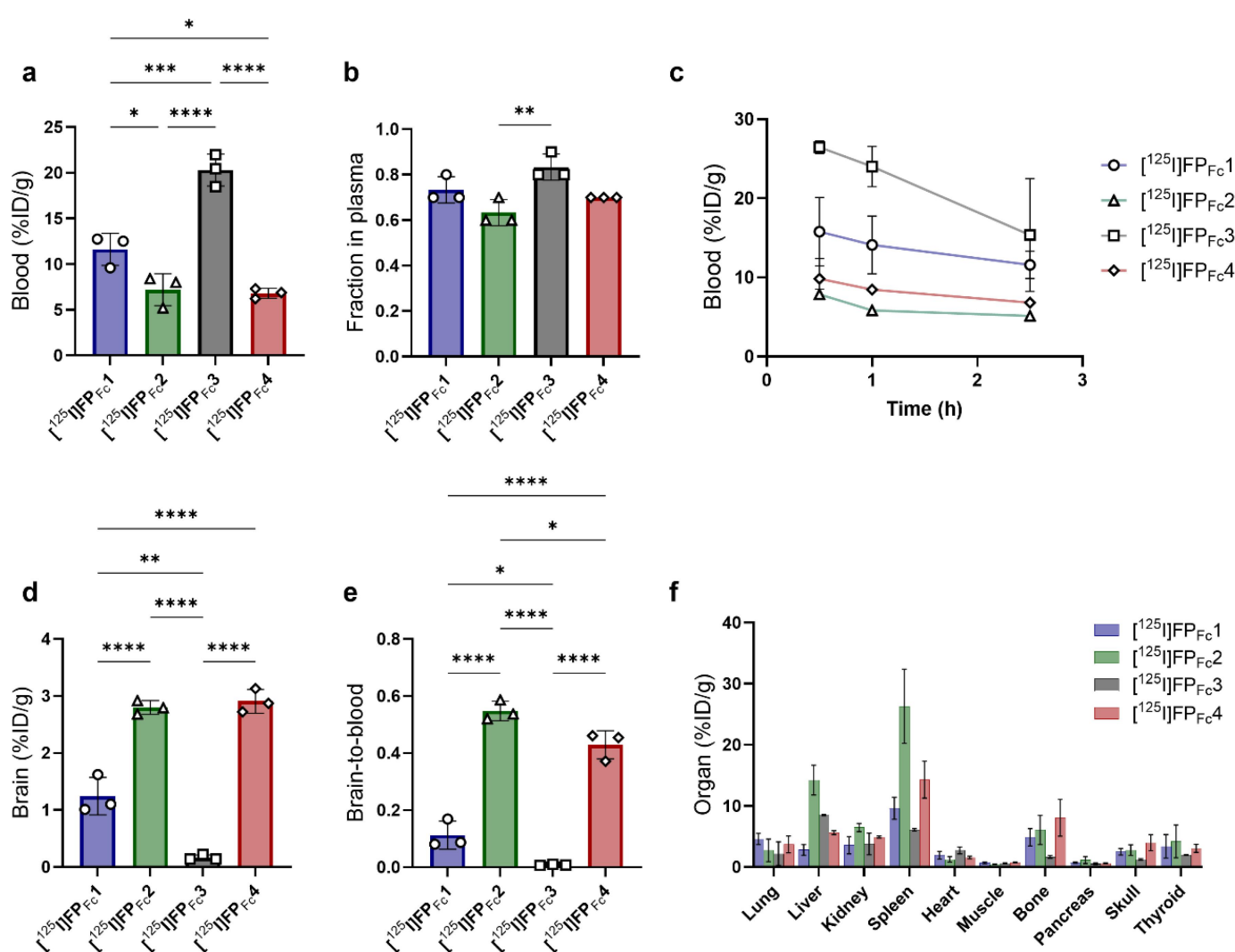


**Figure 3.** Concentrations of fc fusion proteins (FP<sub>Fc</sub>) 2.5 h post administration in WT mice a) blood concentration (%ID/g<sub>blood</sub>) b) fraction of fusion protein in plasma c) blood-time concentration curves (%ID/g<sub>blood</sub>) d) brain concentrations (%ID/g<sub>brain</sub>) e) brain-to-blood ratios and f) biodistribution to peripheral organs for the fc fusion proteins;  $[^{125}\text{I}]\text{FP}_{\text{Fc}1}$ ,  $[^{125}\text{I}]\text{FP}_{\text{Fc}2}$ ,  $[^{125}\text{I}]\text{FP}_{\text{Fc}3}$  and  $[^{125}\text{I}]\text{FP}_{\text{Fc}4}$ .

The brain-to-blood ratio was fairly similar for all FP<sub>scFv</sub> constructs, except for  $[^{125}\text{I}]\text{FP}_{\text{scFv}1\text{A}}$  and  $[^{125}\text{I}]\text{FP}_{\text{scFv}3\text{B}}$  which exhibited lower ratios due to low or no mTfR binding (Figure 6d). In line with what was observed for the FP<sub>Fc</sub> constructs, biodistribution to the spleen was elevated

compared to other peripheral organs for the FP<sub>scFv</sub> constructs (Figure 6e). Autoradiography confirmed the previous *ex vivo* analyses of brain delivery with highest brain concentrations in  $[^{125}\text{I}]\text{FP}_{\text{scFv}2\text{A}}$  and  $[^{125}\text{I}]\text{FP}_{\text{scFv}2\text{B}}$  administered mice (Figure 6f).

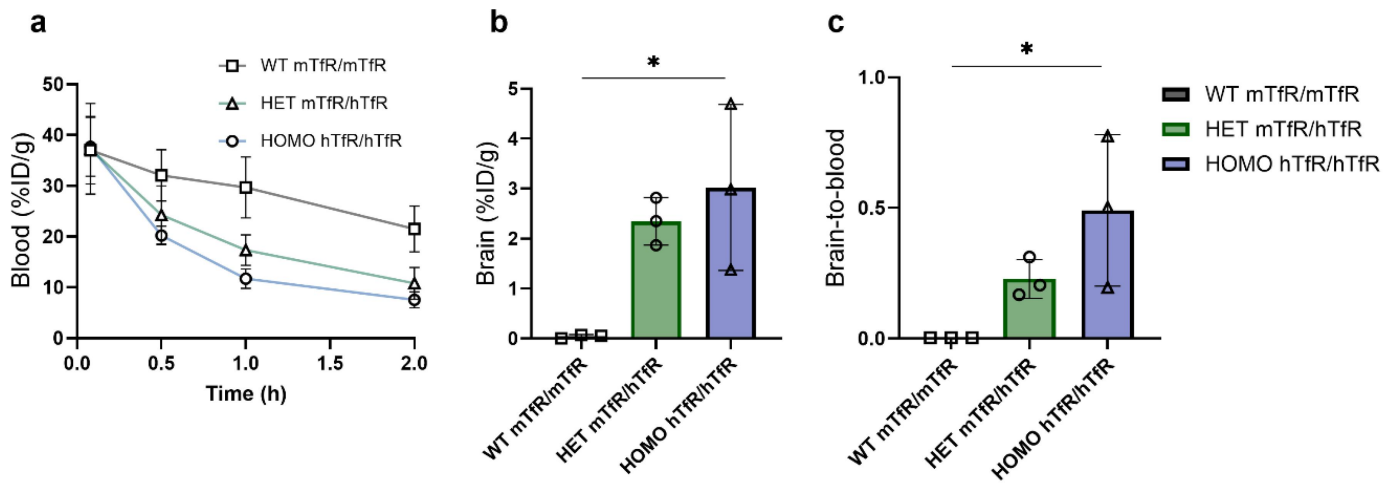


**Figure 4.** a) blood concentrations of human TfR (hTfR) binder FP<sub>c3</sub> in WT mice homozygous for mTfR, mice heterozygous for hTfR and homozygous for hTfR. b) brain concentrations (%ID/g<sub>brain</sub>) and c) brain-to-blood ratios.

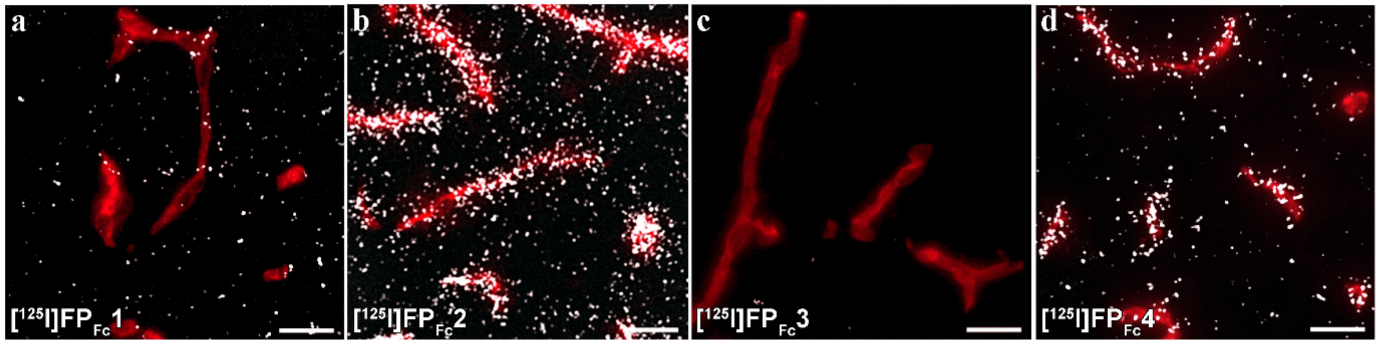


**Figure 5.** a–d) Representative images of nuclear track emulsion autoradiography illustrating the radioactivity (white) in sagittal brain sections from mice 2.5 h post-injection of [<sup>125</sup>I]FP<sub>c1</sub>, [<sup>125</sup>I]FP<sub>c2</sub>, [<sup>125</sup>I]FP<sub>c3</sub> or [<sup>125</sup>I]FP<sub>c4</sub> together with staining of vascular marker CD31 (red). Scale bar = 20 μm.

Taken together, the VHH-scFv (“B-orientation”) showed significantly higher brain concentrations compared with their scFv-VHH counterparts (“A-orientation”).

### Characterization of brain distribution of scFv3d6-fusion proteins

The relative distribution between capillaries and brain parenchyma was further studied with nuclear track emulsion (NTE, microautoradiography) and CD31-immunostaining for [<sup>125</sup>I]FP<sub>scFv1B</sub>, [<sup>125</sup>I]FP<sub>scFv2B</sub> and [<sup>125</sup>I]FP<sub>scFv4B</sub> (Figure 7 a–c). Although the overall brain concentrations were lower for the scFv3D6-fusions compared to the Fc-fusions, the relative levels in the capillary and parenchyma did not differ between FP<sub>Fc</sub> constructs and the FP<sub>scFv</sub> constructs. [<sup>125</sup>I]FP<sub>scFv1B</sub> displayed a relative distribution to the parenchyma vs vasculature of 78%±6%, which was higher than that seen for [<sup>125</sup>I]FP<sub>scFv2B</sub> (60±5%) and [<sup>125</sup>I]FP<sub>scFv4B</sub> (52%±10%) (Figure 7d).

### Ex vivo evaluation of scFv3D6-fusion proteins at 24 h post-injection

The blood and brain retention of the FP<sub>scFv</sub> constructs in WT and *App*<sup>NL-G-F</sup> mice were investigated at 24 h post-injection. In

general, there were no significant differences in blood concentrations (Figure 8a) or fraction in plasma (Figure 8b) between WT and *App*<sup>NL-G-F</sup> mice, for any of the constructs. Blood concentration curves showed that [<sup>125</sup>I]FP<sub>scFv4B</sub>, [<sup>125</sup>I]FP<sub>scFv2A</sub>, and [<sup>125</sup>I]FP<sub>scFv2B</sub> appeared to display slightly slower blood elimination compared to [<sup>125</sup>I]FP<sub>scFv1A</sub>, [<sup>125</sup>I]FP<sub>scFv1B</sub> and [<sup>125</sup>I]FP<sub>scFv4A</sub> (Figure 8c), corroborating results from the 2 h terminal blood samples in WT mice. All FPs, except [<sup>125</sup>I]FP<sub>scFv1A</sub> (*p* = 0.07), displayed significantly higher brain retention in *App*<sup>NL-G-F</sup> mice compared to WT mice, as indicated by both brain concentrations (Figure 8e) and brain-to-blood ratios (Figure 8f). Autoradiography of sagittal brain sections confirmed the genotype-related difference in brain accumulation, which illustrated higher retention in *App*<sup>NL-G-F</sup> mice compared with WT, for [<sup>125</sup>I]FP<sub>scFv1A</sub>, [<sup>125</sup>I]FP<sub>scFv1B</sub>, [<sup>125</sup>I]FP<sub>scFv2A</sub>, [<sup>125</sup>I]FP<sub>scFv2B</sub>, [<sup>125</sup>I]FP<sub>scFv4A</sub> and [<sup>125</sup>I]FP<sub>scFv4B</sub>, and low retention for [<sup>125</sup>I]FP<sub>scFv3B</sub> in *App*<sup>NL-G-F</sup>, indicating retention associated with genotype (Figure 8f, Supplementary Table S2). The difference in brain concentration between WT and *App*<sup>NL-G-F</sup> was greatest, 17-fold, for [<sup>125</sup>I]FP<sub>scFv1B</sub> compared to 7.6 and 11 for the other mTfR active FPs of the “B-orientation”, [<sup>125</sup>I]FP<sub>scFv2B</sub> and [<sup>125</sup>I]FP<sub>scFv4B</sub>, respectively (Supplementary Table S2).

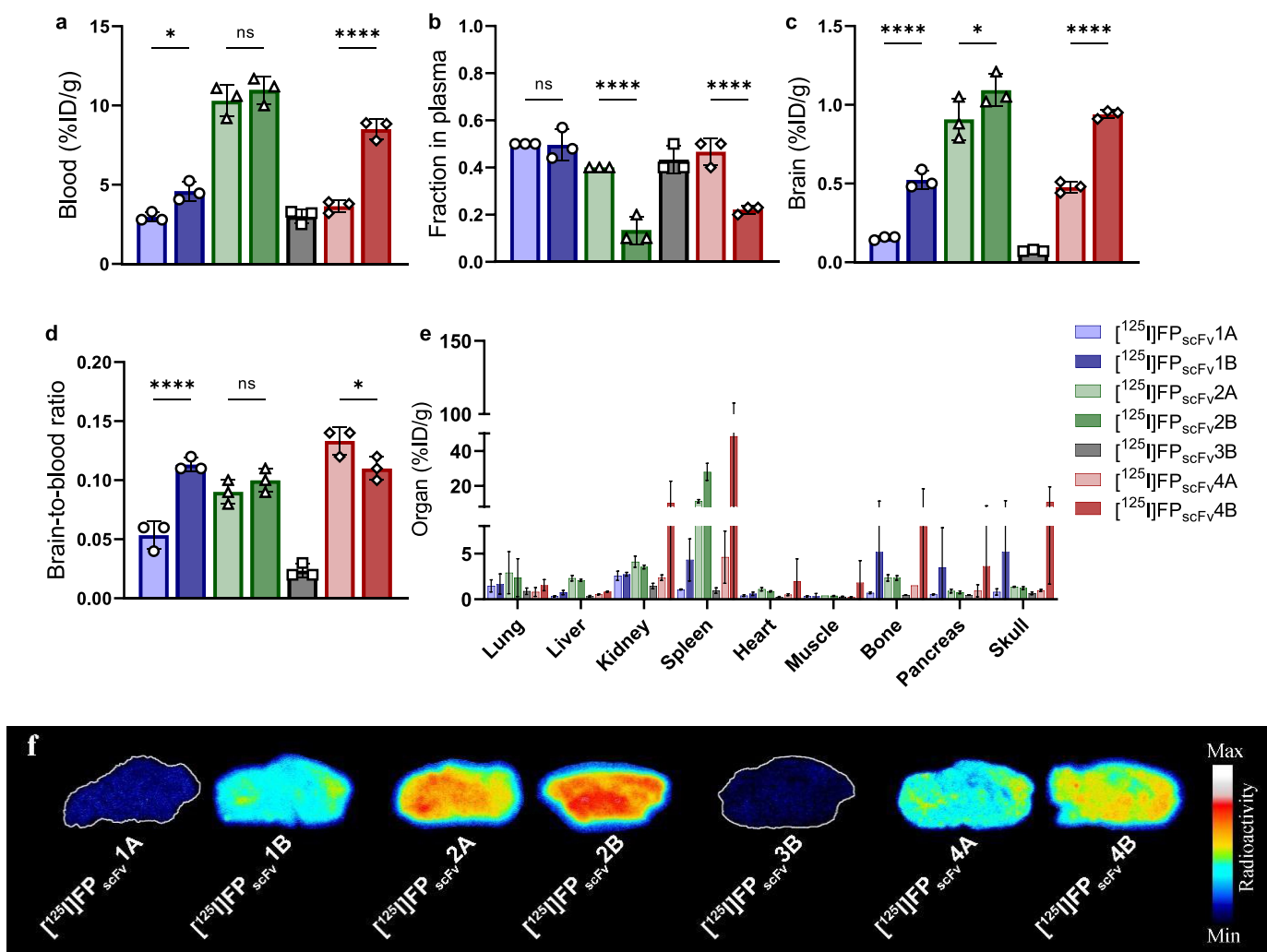


**Figure 6.** Ex vivo evaluation of FP<sub>scFv</sub> constructs in WT mice 2 h post-injection of [<sup>125</sup>I]FP<sub>scFv</sub>1A (light blue), [<sup>125</sup>I]FP<sub>scFv</sub>1B (dark blue), [<sup>125</sup>I]FP<sub>scFv</sub>2A (light green), [<sup>125</sup>I]FP<sub>scFv</sub>2B (dark green), [<sup>125</sup>I]FP<sub>scFv</sub>3B (gray), [<sup>125</sup>I]FP<sub>scFv</sub>4A (light red) or [<sup>125</sup>I]FP<sub>scFv</sub>4B (dark red) a) terminal blood concentration (%ID/g<sub>blood</sub>) b) fraction of fusion protein in plasma c) brain concentration (%ID/g<sub>brain</sub>) d) brain-to-blood ratio e) organ biodistribution and f) representative autoradiography brain sections for <sup>125</sup>I-labeled FP<sub>scFv</sub> constructs in WT mice.

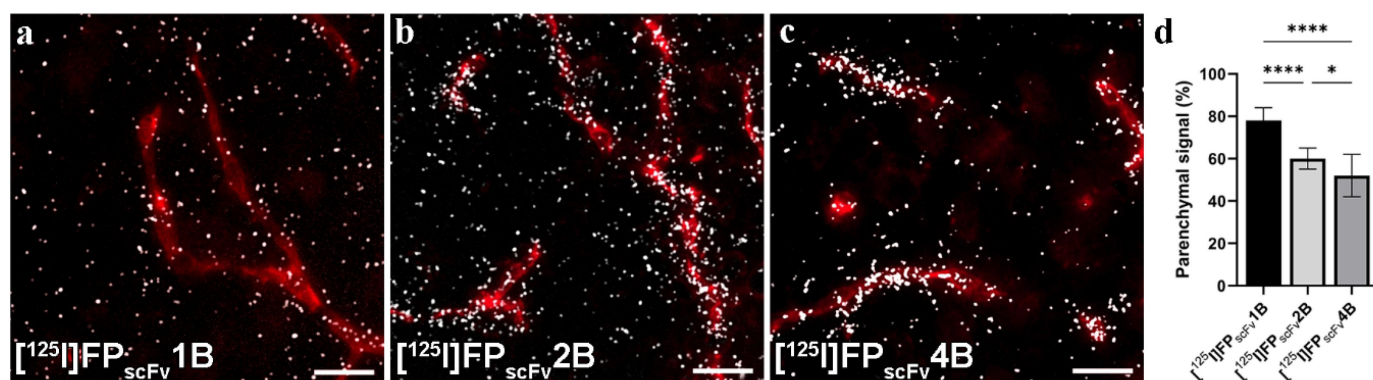


**Figure 7.** Representative images of nuclear track emulsion autoradiography illustrating the radioactivity (white) in sagittal brain sections from mice 2 h post-injection of a) [<sup>125</sup>I]FP<sub>scFv</sub>1B, b) [<sup>125</sup>I]FP<sub>scFv</sub>2B, or c) [<sup>125</sup>I]FP<sub>scFv</sub>4B, together with staining of vascular marker CD31 (red). d) quantification of the percentage of radioactive signal in parenchymal areas for [<sup>125</sup>I]FP<sub>scFv</sub>1B, [<sup>125</sup>I]FP<sub>scFv</sub>2B and [<sup>125</sup>I]FP<sub>scFv</sub>4B. Scale bar = 20 μm.

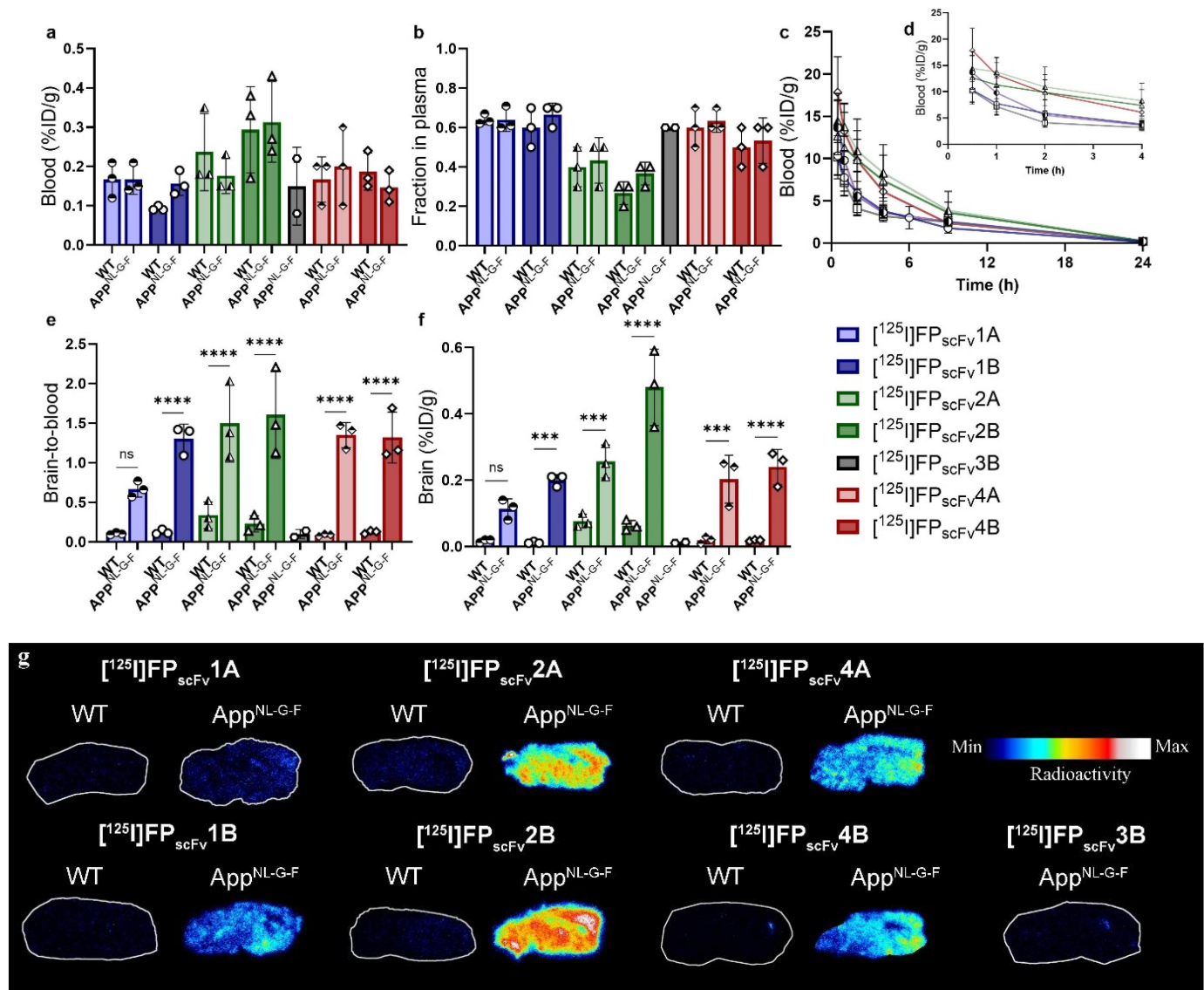


**Figure 8.** Ex vivo evaluation of fusion proteins (FP) in WT and *App<sup>NL-GF</sup>* mice 24 h post-injection of [<sup>125</sup>I]FP<sub>scFv</sub>1A, [<sup>125</sup>I]FP<sub>scFv</sub>1B, [<sup>125</sup>I]FP<sub>scFv</sub>2A, [<sup>125</sup>I]FP<sub>scFv</sub>1B, [<sup>125</sup>I]FP<sub>scFv</sub>3B, [<sup>125</sup>I]FP<sub>scFv</sub>4A or [<sup>125</sup>I]FP<sub>scFv</sub>4B a) terminal blood concentration (%ID/g<sub>blood</sub>) b) fraction of FP in plasma, c) blood-time concentration (%ID/g<sub>brain</sub>) curves during 24 h d) and during initial 4 h post injection e) brain-to-blood ratios f) brain concentrations (%ID/g<sub>brain</sub>) and g) representative autoradiography brain sections for [<sup>125</sup>I]-labeled FPs in WT and *App<sup>NL-GF</sup>* mice.

### Ex vivo evaluation of [<sup>125</sup>I]FP<sub>scFv</sub>1B and [<sup>125</sup>I]FP<sub>scFv</sub>2B at 6 h post-injection

The B-orientations of the FP1 and FP2 fusions, [<sup>125</sup>I]FP<sub>scFv</sub>1B and [<sup>125</sup>I]FP<sub>scFv</sub>2B, respectively, were also studied 6 h post-injection to evaluate their potential to detect brain A $\beta$  at an early time point, which could be relevant for a diagnostic radioligand. In line with the results at 24 h post-injection, *App<sup>NL-GF</sup>* mice displayed higher brain concentrations than WT mice at this time point, albeit with a smaller difference compared to 24 h; 2.5-fold and 1.5-fold for [<sup>125</sup>I]FP<sub>scFv</sub>1B and [<sup>125</sup>I]FP<sub>scFv</sub>2B, respectively (Figure 9a–b). The cross-species reactive [<sup>125</sup>I]FP<sub>scFv</sub>1B was further studied by NTE showing that [<sup>125</sup>I]FP<sub>scFv</sub>1B was associated with both A $\beta$  pathology and to some extent also with the brain vasculature at 6 h post-administration. (Figure 9c–d).

### Discussion

Biologics are emerging as promising therapeutics and diagnostics for the brain. However, their delivery across the BBB is highly restricted, which makes targeting brain-abundant proteins such as A $\beta$  difficult. Therefore, it is crucial to develop strategies that facilitate their transport to the brain. The TfR has been used for this purpose, serving as a shuttle for various biological molecules into the brain.<sup>6,17,20,26,33–36</sup> Moreover, a bispecific antibody directed toward A $\beta$  and TfR (trontine-mab; RO7126209)<sup>37</sup> has been evaluated in a Phase 1/2 study (NCT04639050). There remains, however, a need for small TfR-binders that are easy to express as fusions with the desired therapeutic or diagnostic molecules. In this study, three new TfR-binding VHH proteins, along with one previously described cross-species reactive mouse/human TfR-binding

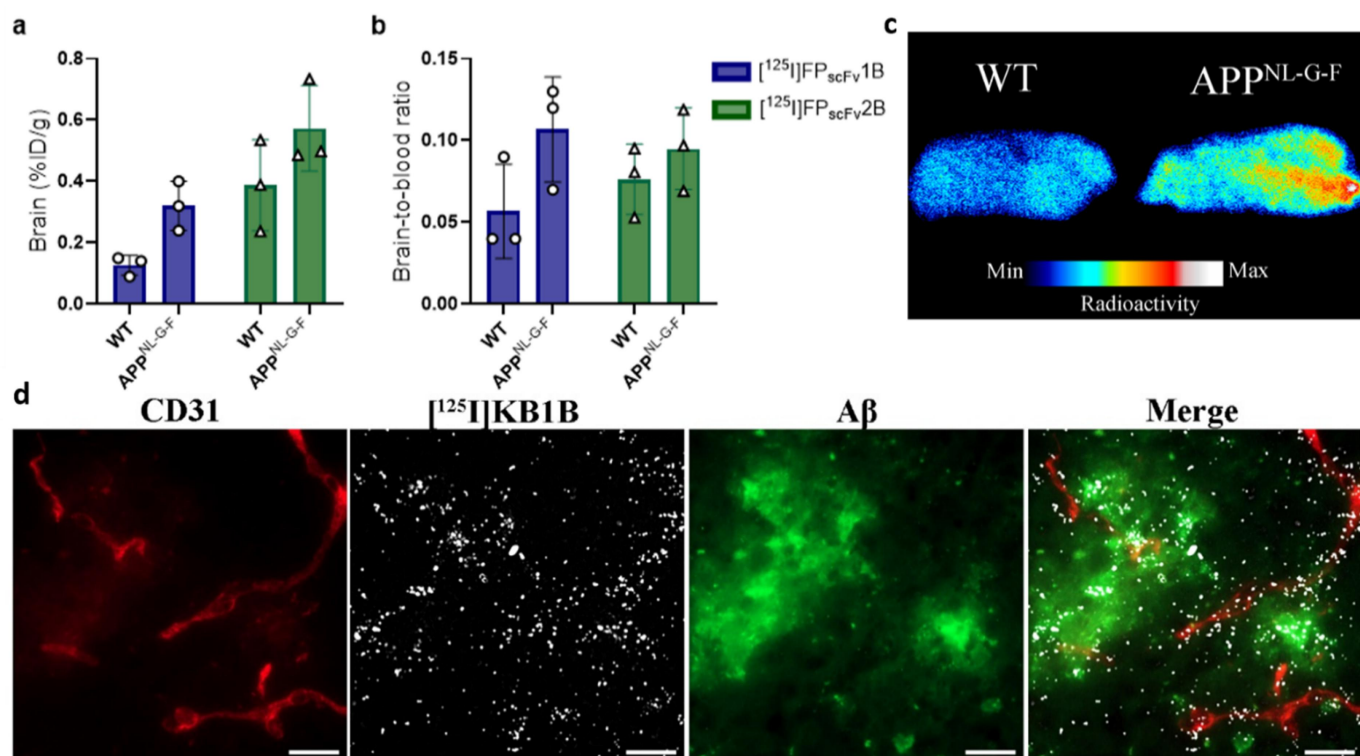


**Figure 9.** *Ex vivo* evaluation of [ $^{125}\text{I}$ ]FP<sub>scFv1B</sub> [ $^{125}\text{I}$ ]FP<sub>scFv2B</sub> in WT and *App*<sup>NL-GF</sup> 6 h post-injection, a) brain concentrations %ID/g<sub>brain</sub> b) brain-to-blood ratio, c) representative autoradiography brain sections for [ $^{125}\text{I}$ ]FP<sub>scFv1B</sub>, showing increased retention in *App*<sup>NL-GF</sup> mice d) nuclear track emulsion of [ $^{125}\text{I}$ ]FP<sub>scFv1B</sub> in *App*<sup>NL-GF</sup> mouse brain, 6 h post-administration. Scale bar = 20  $\mu\text{m}$ .

VHH, were fused to either a human Fc domain or an A $\beta$ -specific scFv, scFv3D6, creating novel FPs. *In vitro* binding assays, including ELISA and SPR, confirmed that VHH1 and VHH4 in both their Fc and scFv fusions bound to both mTfR and hTfR. As expected, the Fc fusions, which exhibited bivalent TfR binding, showed stronger avidity toward the TfR compared to the monovalent binding scFv fusions.

*In vivo*, when the three new VHHs were fused to an Fc domain as bivalent proteins, the mTfR-specific FP<sub>Fc2</sub> demonstrated higher brain distribution compared to the cross-species reactive binder FP<sub>Fc1</sub>. The hTfR binder FP<sub>Fc3</sub> exhibited very low total brain concentration, aligning with previously described brain concentrations for a VHH devoid of TfR-mediated BBB transport.<sup>20</sup> This confirmed that FP<sub>Fc3</sub> was unable to cross the BBB in WT mice, but efficiently crossed the BBB in hTfR-expressing mice. In NTE, FP<sub>Fc2</sub> showed the highest retention in brain capillaries compared to the other FPs, indicating that a high total brain concentration, as measured by total radioactivity, does not necessarily equate to a high concentration in the brain parenchyma. Indeed, previous studies have suggested that low to moderate TfR affinity is preferable for optimal parenchymal delivery.<sup>31,38</sup> These *in vivo* results were largely consistent with the measured *in vitro* affinities, showing that FP<sub>Fc2</sub> had a higher affinity toward mTfR than FP<sub>Fc1</sub>, and that the selective hTfR binder, FP<sub>Fc3</sub>, showed no affinity toward mTfR but high affinity toward hTfR.

All VHH proteins were also fused to the A $\beta$ -binding scFv3D6. In line with initial studies of the Fc fusions, high mTfR affinity correlated with high total brain concentrations

of scFv3D6 fusions at 2 h post-administration, as well as a higher fraction found in brain capillaries as measured by NTE. However, total brain concentrations were generally lower for FP<sub>scFv</sub> constructs compared to FP<sub>Fc</sub> constructs, likely due to reduced avidity for TfR in the monovalent format and potentially lower blood concentrations for scFv fusions compared to the larger Fc fusions. It appeared that VHH fusion to the N-terminus of scFv3D6 (“B-orientation”) resulted in higher brain concentrations compared with fusion to the C-terminus (“A-orientation”), a finding particularly notable for the cross-species reactive FP<sub>scFv1B</sub>. While FP<sub>scFv1B</sub> showed somewhat lower brain concentrations than FP<sub>scFv4B</sub>, it demonstrated greater relative distribution to the parenchyma and was less associated with capillaries at 2 h. Lower TfR affinity of VHH1-based fusions, compared to others, might facilitate dissociation from TfR within the endosomes of brain endothelial cells, allowing for more efficient transcytosis.<sup>31</sup> *In vitro*, FP<sub>scFv1B</sub> and FP<sub>scFv4B</sub> had similar association rate constants to hTfR, but FP<sub>scFv1B</sub> had a nearly 4-fold higher dissociation rate constant ( $k_d$ ) and a 4-fold higher total  $K_D$  compared to FP<sub>scFv4B</sub> in SPR measurements, indicating that the lower affinity may result from faster dissociation from the receptor.

The B-orientation variants, especially FP<sub>scFv1B</sub> and FP<sub>scFv4B</sub>, showed a greater difference between mice with and without A $\beta$  pathology compared to their A-orientation variants. This characteristic is crucial for potential future applications as diagnostic radioligands. Therefore, two N-terminal fusions, FP<sub>scFv1B</sub> and FP<sub>scFv2B</sub>, were also studied 6 h post-injection, with FP<sub>scFv1B</sub> showing a somewhat larger difference

between AD and WT mice, likely due to faster clearance of the unbound construct from the blood and brain.

Thus, for both Fc and scFv fusions, the total brain concentration was highly correlated with affinity toward mTfR; high mTfR affinity resulted in high total brain concentration. However, high mTfR affinity also resulted in a higher fraction of the fusion protein being associated with brain capillaries. In blood, TfR affinity affected elimination, likely due to TfR-mediated clearance in the periphery.<sup>39</sup> However, the impact differed for Fc and scFv fusions. For Fc fusions, high mTfR affinity was associated with fast elimination, while for scFv fusions, high mTfR affinity was associated with slower elimination. This apparent contradiction can be explained by the different molecular sizes of the Fc and scFv fusions. Smaller scFv fusions inherently clear faster. When fused to TfR binders, higher affinity increases their blood residence time. For larger Fc fusions, where the Fc domain itself prolongs residence time in the blood,<sup>40</sup> TfR-mediated clearance increases elimination. Thus, high TfR affinity promotes elimination. This phenomenon has also been demonstrated with full-sized IgG antibodies, which show faster elimination when fused to high-affinity TfR binders.<sup>5,36,41</sup> Another factor that may influence the “optimal” TfR affinity for brain delivery is the nature of the cargo itself. It is important that the affinity for TfR is lower than the cargo’s affinity for the target protein within the brain, such as A $\beta$  in the case of the scFv fusions used in this study. Otherwise, there is a risk that the FPs may bind to TfR on neurons or other cells instead of targeting the intended protein.<sup>17</sup>

We did not measure TfR expression levels in this study. In theory, the amount of TfR could potentially influence both the delivery and the brain retention of the FPs. We have observed increased brain delivery of TfR-targeted bispecific FPs along with increased protein levels of TfR in young mice compared to old.<sup>42</sup> Thus, we used aged-matched AD and WT animals for the 6 h and 24 h brain retention studies. There are conflicting reports on how A $\beta$  pathology may influence the expression of TfR. One study reported no changes in the 3 $\times$ Tg-AD mouse model or in human brain samples.<sup>43</sup> However, another study reported no changes in TfR levels measured in isolated microvessels, but increased expression of TfR in cortical samples from the 5 $\times$ FAD mouse model.<sup>44</sup> In our own previous studies, which align with the report of no changes in TfR expressed at the BBB, we did not observe any difference in the initial brain delivery between AD and WT mice.<sup>42</sup> However, in line with the reports of increased TfR in whole cortical samples that include parenchymal cells, we cannot completely rule out that a fraction of the retention of the scFv fusions at later time points may arise from binding to TfR in parenchymal cells, such as neurons or astrocytes. Yet, this contribution to total brain concentrations is likely to be small, as studies with bispecific antibodies directed toward TfR and a brain irrelevant target do not accumulate more in AD mice than in WT mice.<sup>12,45</sup>

In summary, we have produced and evaluated novel VHH TfR binding fusion proteins, including human-mouse TfR cross-species reactive binders successfully fused with an A $\beta$ -binder, scFv3D6. This enabled transport across the BBB and interaction with A $\beta$  pathology. Although high affinity leads to

higher association with brain tissue, it also results in increased retention in brain capillaries and a lower fraction of the fusion protein in plasma. These processes likely reduce parenchymal distribution, indicating that lower affinity may be desirable for brain delivery. Additionally, low capillary retention and fast clearance from blood, as observed for FP<sub>scFv</sub>1B, reduce background radioactivity, which is important for a diagnostic radioligand. Therefore, it is likely that for a given bispecific TfR-binding fusion format, an optimal affinity window exists where parenchymal delivery is adequate, while blood pharmacokinetics align.

## Materials and methods

### Production of fusion proteins

The four FP<sub>Fc</sub> were expressed in Expi293<sup>TM</sup> cells at Thermo Fisher Scientific, using a murine kappa IgG light-chain signal peptide and purified using standard protein A-based systems.

The FP<sub>scFv</sub> were expressed transiently in Chinese hamster ovary (CHO) cells (TurboCHO<sup>TM</sup>) by Genscript Corp. A 6  $\times$  Histidine C-terminal tag enabled HisTag-based protein purification. The orientation and short names of the FP<sub>scFv</sub> are listed in Table 1.

### In vitro characterization

The binding of FPs to mTfR and hTfR was measured with indirect ELISA. Briefly, 96-well plates (Corning Inc.) were coated with 2  $\mu$ g/ml of mTfR or hTfR (soluble ectodomains with N-terminal 6  $\times$  Histidine tags produced transiently in CHO cells), diluted in phosphate-buffered saline (PBS) and incubated at 4°C overnight. Blocking with 1% bovine serum albumin (BSA) in PBS was performed the following day for 2 h, after which the FPs were serially diluted (1:5) on the plate starting at 250 nM and incubated overnight at 4°C. The plates were incubated for 1 h with horseradish peroxidase (HRP) conjugated anti-VHH antibody (GenScript), and the plates were subsequently developed with K Blue Aqueous TMB substrate (Neogen Corp., Lexington, KY, USA). The reaction was stopped after 10 min with 1 M H<sub>2</sub>SO<sub>4</sub>, and optical density at 450 nm was measured using a spectrophotometer. Fusion antibody and secondary antibody sample dilutions were made in ELISA incubation buffer (PBS, 0.1% BSA, 0.05% Tween-20\*).

The binding of FPs to hTfR and mTfR was also assessed by SPR in single-cycle kinetics mode using a Biacore 8K instrument (Cytiva). For each construct, 5 nM of FP<sub>Fc</sub>, diluted in assay buffer (PBS supplemented with 0.05% Tween-20) were loaded on a protein A chip (Cytiva) for 60 s at 10  $\mu$ L/min followed by exposure to increasing concentration of receptor. Human TfR binding was assessed at a concentration range from 0.078 to 20 nM (five concentrations in four-fold increments) and the mTfR from 0.16 to 40 nM. Contact time for each concentration was 300 s at 30  $\mu$ L/min and dissociation was monitored for 1800 s. After each full five-concentration run, the surface was restored in a single regeneration step by injection of 10 mM glycine at pH 2.0 for 30 s at 30  $\mu$ L/min.

For the FP<sub>scFv</sub> constructs, the receptors hTfR and mTfR were immobilized to a CM5 chip (Cytiva) by amine-coupling using standard methods. FP<sub>scFv</sub>1A/B, FP<sub>scFv</sub>2A/B, and FP<sub>scFv</sub>3A/B were tested to the hTfR at a concentration range of 0.25 to 64 nM (five concentrations in four-fold increments), whereas FP<sub>scFv</sub>1A/B was tested at a concentration range from 0.08 to 50 nM (five concentrations in five-fold increments). FP<sub>scFv</sub>1A/B and FP<sub>scFv</sub>2A/B were also assessed at the mTfR using the same conditions, but at a concentration range from 0.5 to 128 nM (five concentrations in four-fold increments). The contact time for each concentration was 120 s at 30  $\mu$ L/min, and dissociation was monitored for 600 s. After each full five-concentration run, the surface was restored in a single regeneration step by injection of 500 mM MgCl<sub>2</sub> for 30 s at 30  $\mu$ L/min.

The data with respect to the association rate constant ( $k_a$ ), dissociation rate constant ( $k_d$ ) and equilibrium dissociation constant ( $K_D$ ) was evaluated using Biacore Insight Evaluation package (Cytiva) applying a Langmuir 1:1 model.

### Radiochemistry

For *in vivo* evaluation FPs were radiolabeled with iodine-125 (<sup>125</sup>I) using the chloramine T method as previously described.<sup>42,46</sup> Briefly, 15–80  $\mu$ g of FP was mixed with 260  $\pm$  26 kBq/ $\mu$ g for FP<sub>Fc</sub> or 61  $\pm$  2.4 kBq/ $\mu$ g for FP<sub>scFv</sub>, of stock <sup>125</sup>I (PerkinElmer Inc, Waltham, MA, USA) and 5  $\mu$ g of Chloramine T (Sigma Aldrich) in PBS. The reaction (110  $\mu$ L) was allowed to incubate for 90 s before it was quenched with 10  $\mu$ g of Na-metabisulfite (Sigma-Aldrich). The radiolabeled sample was immediately purified with a Zeba-column (ThermoFisher) of 7 kDa cutoff.

### Animals

Experiments to assess brain delivery of the FP<sub>Fc</sub>s and FP<sub>scFv</sub>s were carried out in 3-month-old male WT C57/BL6 mice ( $n = 33$ ). The hTfR binding FP<sub>Fc</sub>3 was also studied in mice with a chimeric ectodomain of hTfR generated by Taconic Biosciences GmbH, in which the endogenous *Tfrc* gene was partially humanized so that the engineered mice produced a chimeric TFRC protein containing the human TFRC extracellular domain, a genotype previously described in literature.<sup>29</sup> Mice were used as both

heterozygotes, homozygotes, and WT littermates ( $n = 3$  per genotype). The pharmacokinetics and brain retention of FP<sub>scFv</sub>s were studied in 13–15 months old *App*<sup>NL-G-F</sup> mice, expressing amyloid precursor protein (APP) gene with a humanized A $\beta$  sequence and with the Swedish (KM670/671NL), Arctic (E693G), and Iberian (I716F) mutations, and in aged-matched WT mice. The *App*<sup>NL-G-F</sup> model is a knock-in model that develops plaque pathology at the age of 2–3 months.<sup>47</sup> Both males ( $n = 25$ ) and females ( $n = 26$ ) were used in the FP<sub>scFv</sub> experiments. All animals used in the study are given in Table 3.

Animals were housed in an animal facility at Uppsala University, with *ad libitum* access to food and water. All experimental procedures described were approved by the Uppsala County Animal Ethics board (5.8.18–20401/20), according to regulations of the Swedish Animal Welfare Agency, and complied with the European Communities Council Directive of 22 September 2010 (2010/63/EU).

### In vivo brain delivery and retention

Immediately following radiolabeling, FP<sub>Fc</sub> (5 nmol/kg; 3.4 MBq/nmol) or FP<sub>scFv</sub> (5 nmol/kg; 6.8 MBq/nmol) were administered as an intravenous injection to mice via the tail vein. To investigate brain targeting, mice were euthanized at 2.5 h post-injection by sampling blood from the heart before transcardial perfusion with 40 mL NaCl (room temperature) for 2.5 min. The brain and major organs were isolated. Blood was separated into plasma and blood-cell pellet by centrifugation at 10 000 g for 5 min. The brain was separated into the left and right hemispheres. The cerebellum was removed from the left hemisphere, and the remaining tissue of the left hemisphere is hereafter referred to as “brain”. Radioactivity was then measured in blood, plasma, blood cell pellet, the right hemisphere, brain, cerebellum, and major organs using a  $\gamma$ -counter (2480 Wizard<sup>TM</sup>, Wallac Oy PerkinElmer, Turku, Finland). To investigate brain retention and pharmacokinetics in blood, both WT and *App*<sup>NL-G-F</sup> mice were administered with the radiolabeled FP. Blood samples (8  $\mu$ L) were obtained from the tail vein at 5 min, 0.5 h, 1 h, 2 h, 4 h, and, if not euthanized at 6 h, at 9 h post injection. At 6 h or 24 h, mice were euthanized, and samples were collected according to the same procedure as described above.

**Table 3.** Fusion proteins, VHH reactivity, and the number of mice injected with respective FP in the study.

Fusion Protein	VHH-Reactivity	WT 3 months	WT/HET/HOMO* 2-3 months	WT 13-15 months	<i>App</i> <sup>NL-G-F</sup> 13-15 months
FP <sub>Fc</sub> 1	mTfR/hTfR	3			
FP <sub>Fc</sub> 2	mTfR	3			
FP <sub>Fc</sub> 3	hTfR	3	3/3/3		
FP <sub>Fc</sub> 4	mTfR/hTfR	3			
FP <sub>scFv</sub> 1A	mTfR/hTfR	3		3	3
FP <sub>scFv</sub> 1B	mTfR/hTfR	3		6	6
FP <sub>scFv</sub> 2A	mTfR	3		3	3
FP <sub>scFv</sub> 2B	mTfR	3		6	6
FP <sub>scFv</sub> 3B	hTfR	3			3
FP <sub>scFv</sub> 4A	mTfR/hTfR	3		3	3
FP <sub>scFv</sub> 4B	mTfR/hTfR	3		3	3

Note: \*Mice from breeding of hTfR expressing mice.

### Ex vivo autoradiography

To visualize the spatial distribution of the radiolabeled FPs in the brain tissue, isolated right hemispheres isolated were sectioned using a Cryostar N×70 (ThermoFisher). Sagittal cryosections (20 µm) were placed in an X-ray cassette along with standards of known <sup>125</sup>I-radioactivity and exposed to a phosphor imaging screen (MS, MultiSensitive, PerkinElmer, Downers grove, IL, USA). The radioactive samples were exposed for seven days and were then scanned in a Cyclone Plus Imager system (Perkin Elmer), at 600 dpi. The resulting digital images were converted to a false color scale (Royal) with ImageJ and normalized to the standards.

### Immunostaining with CD31 and nuclear track emulsion

To investigate the FP relative distribution between vasculature and brain parenchyma, sagittal cryosections of 20 µm were prepared from the right-brain hemisphere of mice injected with the <sup>125</sup>I-labeled FP<sub>FC</sub> or FP<sub>scFv</sub> constructs. The sections were fixed for 10 min in ice-cold methanol, washed with PBS, and blocked with 5% normal goat serum. The sections were incubated with PBS 0.1% Tween-20 for 5 min before overnight incubation with primary antibodies rat-anti-mouse CD31 (BD, #553370), and rabbit-anti-Aβ42 (Agrisera, custom production) at 4°C with slow shaking. The following day, sections were washed with PBS and incubated with goat-anti-rat (Alexa 647) and goat-anti-rabbit (Alexa 488) secondary antibodies. The sections were stored in PBS until the NTE procedure (described below) was performed on the same day.

NTE was carried out according to previously published procedures.<sup>4,42</sup> All processes were performed under darkroom conditions with a safelight according to the manufacturer's instructions. Ilford K5 emulsion was melted in a 40°C water bath and prepared as a 50% solution in ultrapure water. The brain sections were submerged in the emulsion for 10 s, followed by air-drying in RT for 2 h. The sections were stored at 4°C, in a light-sealed box for 4 weeks. The development was done according to the manufacturer's instructions. The sections with immunostaining and developed emulsion were visualized with a Zeiss Observer Z.1 microscope using ZEN software (Carl Zeiss Microimaging GmbH, Jena, Germany). The brightfield channel was inverted to show the emulsion grains as white puncta, instead of black, together with the CD31 staining in the red 647-channel.

Quantification of the relative parenchymal vs capillary signal (%Parenchyma) in the NTE images was done using randomly distributed cortical images ( $n = 20$  per animal). Images were taken from one selected animal per group displaying the median brain concentrations. The quantification was performed with a standardized macro in Fiji (ImageJ) as previously described.<sup>9</sup>

### Statistical analyses

All data presented here are shown as mean ± SD. Shapiro-Wilk test and diagnostic plots were used to evaluate the normal distribution of the data. The ELISA data was fitted using saturation binding curves. One-way or two-way ANOVA followed by Bonferroni *post hoc* analyses were applied to correct

for multiple comparisons. Statistically significant differences were defined as:  $p$ -value <0.05 (\*),  $p$ -value <0.01(\*\*),  $p$ -value <0.001(\*\*\*),  $p$ -value <0.0001(\*\*\*\*). Graphs and statistical analyses were performed in GraphPad Prism version 9.4.1 for Windows (GraphPad Software, San Diego, California, USA).

### Acknowledgments

We would like to thank Takashi Saito and Takaomi Saido at RIKEN Center for Brain Science, for the development of the  $App^{NL-G-F}$  model used in the present study. The radioactivity work in this study was performed at the SciLifeLab Pilot Facility for Preclinical PET-MRI, a Swedish nationally available imaging platform at Uppsala University, Sweden, financed by the Knut and Alice Wallenberg Foundation.

### Disclosure statement

Elisabet O Sjöström, Tiffany Dallas, Magnus M Berglund are employees of Key2Brain AB, Sweden. The other authors have no competing interests to declare.

### Funding

Open access funding provided by Uppsala University. This work was supported by Hans-Gabriel och Alice Trolle-Wachtmeisters stiftelse för medicinsk forskning, Grants from the Swedish Research Council (2021-01083 and 2021-03524), the Swedish Innovation Agency, Alzheimerfonden, Hjärnfonden, Torsten Söderbergs stiftelse, Åhlenstiftelsen, Stiftelsen för gamla tjänarinnor, Stohnes stiftelse, Magnus Bergvalls stiftelse, Konung Gustaf V:s och Drottning Victorias frimurarestiftelse and Åke Wibergs stiftelse. The funding bodies did not take part in design of the study, in collection, analysis, or interpretation of data, nor in writing the manuscript.

### ORCID

Dag Sehlin  <http://orcid.org/0000-0002-9430-3859>

Stina Syvänen  <http://orcid.org/0000-0002-8196-4041>

### References

- van Dyck Ch, Swanson CJ, Aisen P, Bateman RJ, Chen C, Gee M, van Dyck CH, Kanekiyo M, Li D, Reyderman L. et al. Lecanemab in early Alzheimer's disease. *N Engl J Med.* 2023;388(1):9–21. doi:10.1056/NEJMoa2212948.
- Budd Haeberlein S, Aisen PS, Barkhof F, Chalkias S, Chen T, Cohen S, Dent G, Hansson O, Harrison K, von Hehn C. et al. Two randomized phase 3 studies of aducanumab in early Alzheimer's disease. *J Prev Alzheimers Dis.* 2022;9:197–210. doi:10.14283/jpad.2022.30.
- Sims JR, Zimmer JA, Evans CD, Lu M, Ardayfio P, Sparks J, Wessels AM, Shcherbinin S, Wang H, Monkul Nery ES. et al. Donanemab in early symptomatic Alzheimer disease: the TRAILBLAZER-ALZ 2 randomized clinical trial. *JAMA.* 2023;330(6):512–527. doi:10.1001/jama.2023.13239.
- Gustavsson T, Syvanen S, O'Callaghan P, Sehlin D. SPECT imaging of distribution and retention of a brain-penetrating bispecific amyloid-β antibody in a mouse model of Alzheimer's disease. *Transl Neurodegener.* 2020;9(1):37. doi:10.1186/s40035-020-00214-1.
- Hultqvist G, Syvanen S, Fang XT, Lannfelt L, Sehlin D. Bivalent brain shuttle increases antibody uptake by monovalent binding to the transferrin receptor. *Theranostics.* 2017;7(2):308–318. doi:10.7150/thno.17155.

6. Kariolis MS, Wells RC, Getz JA, Kwan W, Mahon CS, Tong R, Kim DJ, Srivastava A, Bedard C, Henne KR, et al. Brain delivery of therapeutic proteins using an Fc fragment blood-brain barrier transport vehicle in mice and monkeys. *Sci Transl Med.* 2020; 12. doi:10.1126/scitranslmed.aay1359.
7. Magnusson K, Sehlin D, Syvanen S, Svedberg MM, Philipson O, Soderberg L, Tegerstedt K, Holmquist M, Gellerfors P, Tolmachev V. et al. Specific uptake of an amyloid- $\beta$  protofibril-binding antibody-tracer in A $\beta$ PP transgenic mouse brain. *J Alzheimers Dis.* 2013;37(1):29–40. doi:10.3233/JAD-130029.
8. Bard F, Cannon C, Barbour R, Burke RL, Games D, Grajeda H, Guido T, Hu K, Huang J, Johnson-Wood K. et al. Peripherally administered antibodies against amyloid  $\beta$ -peptide enter the central nervous system and reduce pathology in a mouse model of Alzheimer disease. *Nat Med.* 2000;6(8):916–919. doi:10.1038/78682.
9. Faresjo R, Bonvicini G, Fang XT, Aguilar X, Sehlin D, Syvanen S. Brain pharmacokinetics of two BBB penetrating bispecific antibodies of different size. *Fluids Barriers CNS.* 2021;18(1):26. doi:10.1186/s12987-021-00257-0.
10. Meier SR, Sehlin D, Roshanbin S, Falk VL, Saito T, Saido TC, Neumann U, Rokka J, Eriksson J, Syvänen S. et al. 11 C-PiB and 124 I-Antibody PET provide differing estimates of brain amyloid- $\beta$  after Therapeutic intervention. *J Nucl Med.* 2022;63(2):302–309. doi:10.2967/jnumed.121.262083.
11. Meier SR, Syvanen S, Hultqvist G, Fang XT, Roshanbin S, Lannfelt L, Neumann U, Sehlin D. Antibody-based in vivo PET imaging detects amyloid- $\beta$  reduction in Alzheimer transgenic mice after BACE-1 inhibition. *J Nucl Med.* 2018;59(12):1885–1891. doi:10.2967/jnumed.118.213140.
12. Sehlin D, Fang XT, Cato L, Antoni G, Lannfelt L, Syvanen S. Antibody-based PET imaging of amyloid beta in mouse models of Alzheimer's disease. *Nat Commun.* 2016;7(1):10759. doi:10.1038/ncomms10759.
13. Sehlin D, Syvanen S. Engineered antibodies: new possibilities for brain PET? *Eur J Nucl Med Mol Imag.* 2019;46(13):2848–2858. doi:10.1007/s00259-019-04426-0.
14. Syvanen S, Hultqvist G, Gustavsson T, Gumucio A, Laudon H, Soderberg L, Ingelsson N, Lannfelt L, Sehlin D. Efficient clearance of A $\beta$  protofibrils in A $\beta$ PP-transgenic mice treated with a brain-penetrating bifunctional antibody. *Alzheimers Res Ther.* 2018;10(1):49. doi:10.1186/s13195-018-0377-8.
15. Syvanen S, Meier SR, Roshanbin S, Xiong M, Faresjo R, Gustavsson T, Bonvicini G, Schlein E, Aguilar X, Julku U. et al. PET imaging in preclinical anti-A $\beta$  drug development. *Pharm Res.* 2022;39(7):1481–1496. doi:10.1007/s11095-022-03277-z.
16. Li Z, Krippendorff BF, Shah DK. Influence of molecular size on the clearance of antibody fragments. *Pharm Res.* 2017;34(10):2131–2141. doi:10.1007/s11095-017-2219-y.
17. Faresjo R, Lindberg H, Stahl S, Lofblom J, Syvanen S, Sehlin D. Transferrin receptor binding BBB-Shuttle facilitates brain delivery of anti-A $\beta$ -antibodies. *Pharm Res.* 2022;39(7):1509–1521. doi:10.1007/s11095-022-03282-2.
18. Bao G, Tang M, Zhao J, Zhu X. Nanobody: a promising toolkit for molecular imaging and disease therapy. *EJNMMI Res.* 2021;11(1):6. doi:10.1186/s13550-021-00750-5.
19. Lessard E, Rennie K, Haqqani A, Ling B, Whitfield J, Paradis A, Araujo J, Yoganathan N, Gillard J, Stanimirovic D. et al. Pharmacokinetics and pharmacodynamic effect of a Blood-brain barrier-crossing fusion protein Therapeutic for Alzheimer's disease in rat and dog. *Pharm Res.* 2022;39(7):1497–1507. doi:10.1007/s11095-022-03285-z.
20. Meier SR, Sehlin D, Syvanen S. Passive and receptor mediated brain delivery of an anti-fgap nanobody. *Nucl Med Biol.* 2022;114-115:121–127. doi:10.1016/j.nucmedbio.2022.04.002.
21. Wouters Y, Jaspers T, Rue L, Serneels L, De Strooper B, Dewilde M. VHHs as tools for therapeutic protein delivery to the central nervous system. *Fluids Barriers CNS.* 2022;19(1):79. doi:10.1186/s12987-022-00374-4.
22. Yogi A, Hussack G, van Faassen H, Haqqani AS, Delaney CE, Brunette E, Sandhu JK, Hewitt M, Sulea T, Kemmerich K. et al. Brain delivery of IGF1R5, a single-Domain antibody targeting insulin-like growth factor-1 receptor. *Pharmaceutics.* 2022;14(7):1452. doi:10.3390/pharmaceutics14071452.
23. Niewoehner J, Bohrmann B, Collin L, Urich E, Sade H, Maier P, Rueger P, Stracke J, Lau W, Tissot A. et al. Increased brain penetration and potency of a therapeutic antibody using a monovalent molecular shuttle. *Neuron.* 2014;81(1):49–60. doi:10.1016/j.neuron.2013.10.061.
24. Yu YJ, Atwal JK, Zhang Y, Tong RK, Wildsmith KR, Tan C, Bien-Ly N, Hersom M, Maloney JA, Meilandt WJ. et al. Therapeutic bispecific antibodies cross the blood-brain barrier in nonhuman primates. *Sci Transl Med.* 2014;6(261):261ra154. doi:10.1126/scitranslmed.3009835.
25. Zhao P, Anami Y, Gao P, Fan X, Li L, Tsuchikama K, Zhang N, An Z. Enhanced anti-angiogenic effect of transferrin receptor-mediated delivery of VEGF-trap in a glioblastoma mouse model. *Mabs.* 2022;14(1):2057269. doi:10.1080/19420862.2022.2057269.
26. Cohen R, David M, Khrestchatsky M. Transferrin receptor-binding molecules, conjugates thereof and their uses. In. 2022. <https://patents.google.com/patent/AU2020206593A1/en>
27. Okuyama T, Eto Y, Sakai N, Minami K, Yamamoto T, Sonoda H, Yamaoka M, Tachibana K, Hirato T, Sato Y. et al. Iduronate-2-sulfatase with anti-human transferrin receptor antibody for neuropathic mucopolysaccharidosis II: a phase 1/2 trial. *Mol Ther.* 2019;27(2):456–464. doi:10.1016/j.ymthe.2018.12.005.
28. Sehlin D, Stocki P, Gustavsson T, Hultqvist G, Walsh FS, Rutkowski JL, Syvanen S. Brain delivery of biologics using a cross-species reactive transferrin receptor 1 VNAR shuttle. *Faseb J.* 2020;34:13272–13283. doi:10.1096/fj.202000610RR.
29. Sonoda H, Morimoto H, Yoden E, Koshimura Y, Kinoshita M, Golovina G, Takagi H, Yamamoto R, Minami K, Mizoguchi A. et al. A blood-brain-barrier-penetrating anti-human transferrin receptor antibody fusion protein for neuronopathic mucopolysaccharidosis II. *Mol Ther.* 2018;26(5):1366–1374. doi:10.1016/j.ymthe.2018.02.032.
30. Morrison JI, Metzendorf NG, Rofo F, Petrovic A, Hultqvist G. A single-chain fragment constant design enables easy production of a monovalent blood-brain barrier transporter and provides an improved brain uptake at elevated doses. *J Neurochem.* 2023;165(3):413–425. doi:10.1111/jnc.15768.
31. Yu YJ, Zhang Y, Kenrick M, Hoyte K, Luk W, Lu Y, Atwal J, Elliott JM, Prabhu S, Watts RJ. et al. Boosting brain uptake of a therapeutic antibody by reducing its affinity for a transcytosis target. *Sci Transl Med.* 2011;3(84):84ra44. doi:10.1126/scitranslmed.3002230.
32. Feinberg H, Saldanha JW, Diep L, Goel A, Widom A, Veldman GM, Weis WI, Schenk D, Basi GS. Crystal structure reveals conservation of amyloid- $\beta$  conformation recognized by 3D6 following humanization to bapineuzumab. *Alzheimers Res Ther.* 2014;6(3):31. doi:10.1186/alzrt261.
33. Rofo F, Metzendorf NG, Saubi C, Suominen L, Godec A, Sehlin D, Syvänen S, Hultqvist G. Blood-brain barrier penetrating neprilysin degrades monomeric amyloid-beta in a mouse model of Alzheimer's disease. *Alzheimers Res Ther.* 2022;14(1):180. doi:10.1186/s13195-022-01132-2.
34. Rofo F, Ugur Yilmaz C, Metzendorf N, Gustavsson T, Beretta C, Erlandsson A, Sehlin D, Syvänen S, Nilsson P, Hultqvist G. et al. Enhanced neprilysin-mediated degradation of hippocampal A $\beta$ 42 with a somatostatin peptide that enters the brain. *Theranostics.* 2021;11(2):789–804. doi:10.7150/thno.50263.
35. van Lengerich B, Zhan L, Xia D, Chan D, Joy D, Park JI, Tatarakis D, Calvert M, Hummel S, Lianoglou S, et al. A TREM2-activating antibody with a blood-brain barrier transport vehicle enhances microglial metabolism in Alzheimer's disease models. *Nat Neurosci.* 2023;26:416–429. doi:10.1038/s41593-022-01240-0.
36. Roshanbin S, Julku U, Xiong M, Eriksson J, Masliah E, Hultqvist G, Bergström J, Ingelsson M, Syvänen S, Sehlin D. et al. Reduction of  $\alpha$ SYN pathology in a mouse Model of PD

- using a brain-penetrating bispecific antibody. *Pharmaceutics*. 2022;14(7):1412. doi:10.3390/pharmaceutics14071412.
37. Grimm HP, Schumacher V, Schafer M, Imhof-Jung S, Freskgard PO, Brady K, Hofmann C, Rieger P, Schlothauer T, Göpfert U. et al. Delivery of the Brainshuttle™ amyloid-beta antibody fusion trontinemab to non-human primate brain and projected efficacious dose regimens in humans. *MAbs*. 2023;15(1):2261509. doi:10.1080/19420862.2023.2261509.
  38. Arguello A, Mahon CS, Calvert MEK, Chan D, Dugas JC, Pizzo ME, Thomsen ER, Chau R, Damo LA, Duque J. et al. Molecular architecture determines brain delivery of a transferrin receptor-targeted lysosomal enzyme. *J Exp Med*. 2022;219(3). doi:10.1084/jem.20211057.
  39. Couch JA, Yu YJ, Zhang Y, Tarrant JM, Fuji RN, Meilandt WJ, Solanoy H, Tong RK, Hoyte K, Luk W. et al. Addressing safety liabilities of TfR bispecific antibodies that cross the blood-brain barrier. *Sci Transl Med*. 2013;5(183):183ra157, 181–112. doi:10.1126/scitranslmed.3005338.
  40. Schlein E, Andersson KG, Dallas T, Syvanen S, Sehlin D. Reducing neonatal fc receptor binding enhances clearance and brain-to-blood ratio of TfR-delivered bispecific amyloid- $\beta$  antibody. *MAbs*. 2024;16(1):2339337. doi:10.1080/19420862.2024.2339337.
  41. Julku U, Xiong M, Wik E, Roshanbin S, Sehlin D, Syvanen S. Brain pharmacokinetics of mono- and bispecific amyloid- $\beta$  antibodies in wild-type and Alzheimer's disease mice measured by high cut-off microdialysis. *Fluids Barriers CNS*. 2022;19(1):99. doi:10.1186/s12987-022-00398-w.
  42. Faresjo R, Sehlin D, Syvanen S. Age, dose, and binding to TfR on blood cells influence brain delivery of a TfR-transported antibody. *Fluids Barriers CNS*. 2023;20(1):34. doi:10.1186/s12987-023-00435-2.
  43. Bourassa P, Alata W, Tremblay C, Paris-Robidas S, Calon F. Transferrin receptor-mediated uptake at the blood-brain barrier is not impaired by Alzheimer's disease neuropathology. *Mol Pharm*. 2019;16(2):583–594. doi:10.1021/acs.molpharmaceut.8b00870.
  44. Puris E, Auriola S, Petralla S, Hartman R, Gynther M, de Lange ECM, Fricker G. Altered protein expression of membrane transporters in isolated cerebral microvessels and brain cortex of a rat Alzheimer's disease model. *Neurobiol Dis*. 2022;169:105741. doi:10.1016/j.nbd.2022.105741.
  45. Wuensche TE, Stergiou N, Mes I, Verlaan M, Schreurs M, Kooijman EJM, Janssen B, Windhorst AD, Jensen A, Asuni AA. et al. Advancing 89 Zr-immuno-pet in neuroscience with a bispecific anti-amyloid-beta monoclonal antibody - the choice of chelator is essential. *Theranostics*. 2022;12(16):7067–7079. doi:10.7150/thno.73509.
  46. Greenwood FC, Hunter WM, Glover JS. The preparation of I-131-Labelled human growth hormone of high specific radioactivity. *Biochem J*. 1963;89(1):114–123. doi:10.1042/bj0890114.
  47. Saito T, Matsuba Y, Mihira N, Takano J, Nilsson P, Itohara S, Iwata N, Saido TC. Single app knock-in mouse models of Alzheimer's disease. *Nat Neurosci*. 2014;17:661–663. doi:10.1038/nn.3697.